Experimental Validation of a Bio-Inspired Thruster

(Article begins on next page)

07 January 2025

American Society of Mechanical Engineers

ASME Accepted Manuscript Repository

Experimental Validation of a Bio-Inspired Thruster

Daniele Costa[1]
DIISM, Università Politecnica delle Marche
Department of Industrial Engineering and Mathematical Sciences, Università Politecnica delle Marche, 60131 Ancona, Italy
d.costa@univpm.it

Giacomo Palmieri
DIISM, Università Politecnica delle Marche
Department of Industrial Engineering and Mathematical Sciences, Università Politecnica delle Marche, 60131 Ancona, Italy
g.palmieri@univpm.it

Massimo Callegari
DIISM, Università Politecnica delle Marche
Department of Industrial Engineering and Mathematical Sciences, Università Politecnica delle Marche, 60131 Ancona, Italy
m.callegari@staff.univpm.it
Associate Editor of ASME Journal of Mechanical Design

David Scaradozzi
DII, Università Politecnica delle Marche
Department of Information Engineering, Università Politecnica delle Marche, 60131 Ancona, Italy
d.scaradozzi@staff.univpm.it

ABSTRACT

Bio-inspired solutions have been deeply investigated in the last two decades as a source of propulsive

improvement for Autonomous Underwater Vehicles. Despite the efforts made to pursue the substantial

potential payoffs of marine animals' locomotion, the performances of biological swimmers are still far to

reach. The possibility to design a machine capable of propelling itself like a marine animal strongly

depends on the understanding of the mechanics principles underlying biological swimming. Therefore, the

---

[1] Daniele Costa is the corresponding author.

adoption of advanced simulation and measurement techniques is fundamental to investigate the fluid-structure interaction phenomena of aquatic animals' locomotion. Among those, computational fluid dynamics represents an invaluable tool to assess the propulsive loads due to swimming. However, the numerical predictions must be validated before they can be applied to the design of a bio-inspired robot. To this end, this paper presents the experimental setup devised to validate the fluid dynamics analysis performed on an oscillating foil. The numerical predictions led to the design of a strain gauges-based sensor which exploits the deflection and twisting of the foil shaft to indirectly measure the propulsive loads and obtain a complete dynamic characterization of the oscillating foil. The results obtained from the experiments showed a good agreement between the numerical predictions and the measured loads; the test equipment also allowed to investigate the potential benefits of a slender fish-like body placed before the spinning fin. Therefore, in future work, the system will be employed to validate the analysis performed on more sophisticated modes of locomotion.

1. INTRODUCTION

The comparative biomechanics of moving through water has attracted the attention of biologists and engineers for a long time and the last decades have witnessed a significant growth in the study of aquatic animal locomotion. The attempts to design an Autonomous Underwater Vehicles, AUV, capable of moving like marine mammals and fish, are due to the superior performances of biological swimmers both in terms of efficiency and maneuverability [1], overtaking classical AUV design for specific marine applications [2-4]. Hence, several prototypes of bio-inspired robots, such as those in [5-7], have been manufactured worldwide and an extensive review is given in [1]. The possibility to replicate the swimming modes matured over thousands of years of evolution relies on the understanding of the fluid mechanic principles of aquatic animals' locomotion. By using advanced simulation and measurement techniques,

engineers are trying to quantify the propulsive performances of biological swimmers, such as thrust and efficiency. To this end, computational fluid dynamics analysis (CFD) represents an invaluable tool to estimate the hydrodynamic forces and torque resulting from the fluid-structure interactions occurring during swimming [8,9]. Besides, CFD results are generally expressed as a function of a few non-dimensional parameters which take into account both the geometry and kinematics of the thrusters, namely the swimmer's tail and fins. This feature allows performing only a few long-lasting simulations, thus reducing computational time, and then to apply the predicted solutions to many different scenarios. This possibility has been exploited by the authors in [10], where the numerical results have been coupled to the multibody model of a robotic fish in order to simulate its dynamics – and not just a steady-state cruising condition – in a parametric way. However, before the aforementioned method could be applied, the CFD predictions must be experimentally validated.

According to literature, experimental work has already been conducted both on fin-shaped foils isolated from the robotic fish body [11-13] as well as on fully assembled bio-inspired underwater robots [14-18]. Particularly, two different setups have been devised to investigate the performances of fin-based propulsion. In the former, the swimming robot is either towed at known speed through a water tank or, which is equivalent, placed in a freestream at a given velocity in a water tunnel [15,16]: the propulsive force is then measured by load cells attached to the towing structure. Here, though, the foil kinematics is completely decoupled from the speed of towing or from the freestream velocity, a condition dissimilar from what occurs in biological

locomotion. On the other hand, in the alternative setup, the robot swims at a self-propelled speed on a low-friction guide [17,18]: an average velocity is then reached when thrust balances the drag force exerted by the fluid on the self-propelled vehicle. However, the increase in inertia due to the presence of the additional parts (struts, sliders, etc.) results in a difference of acceleration between the biological swimmer and the robot, hindering the measurement of the hydrodynamic loads acting on the latter's body and the propulsive forces generated by its fin. An exhaustive review of recent advances on self-propelled bodies is given in [19].

This paper presents the experimental validation of the CFD analysis performed on an oscillating foil which spins around its rotation axis following a sinusoidal law of motion, a kinematic condition that closely matches the fin pendulum-like oscillation of ostraciiform swimmers [20]. Compared to other undulatory Body and Caudal Fin modes [1], ostraciiform locomotion is the least efficient but the mechanical system that realizes this propulsion – consisting in a fin-shaped foil hinged to the fore body through a revolute joint – is simple, easy to fabricate and miniaturize.

Ostraciiform swimming vehicles have already been tested in previous works: in [21], a pulley and weight system has been used to generate a constant pull force on the robotic fish. The experiments have been conducted with four different fin shapes and various oscillating frequencies, while the measured added mass and drag coefficients have been compared to a theoretical model. An alternative setup has been devised in [22], where the oscillating fin has been placed in an oil tank: here, a force sensor has

been employed to measure the force components generated by the spinning foil, while

the results have been used to manufacture a robotic boxfish.

Compared to the aforementioned works, the main novelty in this paper is the

attainment of a complete characterization of the oscillating fin, meaning the

measurement of the propulsive forces and torque acting on a centimeter-scale

ostraciiform thruster even in the absence of large and expensive equipment. In fact, the

working dimensions of the water flume used in [9,12,13,15] are 30 m long, 2.5 m wide

and 1.2 m deep. By comparison, the rectangular section of the flume used by the

authors is 330 mm wide and 250 mm deep. Smaller tanks have been also used in

[13,21], but the oscillating fin has been tested in still water to measure its static

performances.

Furthermore, since the expected propulsive forces generated by the spinning foil

tested in this paper are of the order of 10^{-2} N due to size of the available water flume,

the authors have designed a custom force sensor which exploits the deflections and

twisting of a fin shaft to measure the hydrodynamic forces applied to the fin itself. The

measurement is then obtained by means of three independent groups of strain gauges

attached to the shaft as shown in figure 1; thus, the force sensor connects the oscillating

fin with its actuation system, which is fixed to the flume above the water. This assembly

constraints the system in the buoyancy direction, thus neglecting the propulsive effects

of tridimensional motion which actually occurs in real fish swimming. This feature is

beyond the scope of this paper, where the fin motion is constrained to the plane

perpendicular to the vertical direction; still, the effects of tridimensional motion on thrust generation will be deeply investigated in future experimental works.

Strain gauges have been preferred in this paper because of their affordability with respect to load cells capable to operate at low force range like those used in [11-18,22]. Likewise, the possibility to size the fin shaft as a function of the CFD predicted loads allows to adjust the sensor stiffness in order to constrain the corresponding deformations to a range where the strain gauges are sufficiently free from noise disturbances. Lastly, the usage of a load cell installed between the flume and the fin actuation mechanism, as in previous works, would have required the adoption of a carriage-and-guide assembly to support the whole system. However, this constraint would have prevented the measurement of the force component perpendicular to the sliding direction and of the hydrodynamic torque as well. In other words, only the thrust component would have been measured. However, given the periodic behavior of the thrust force, its measurements would have been affected by the inertia force due to the actuation and support system, thus only an average value would have been obtained. On the contrary, the proposed experimental setup allowed the authors to measure the instantaneous values of both force components and propulsive torque in the oscillation cycle, also avoiding that friction and system inertia would affect the measurements.

On the basis of the former discussion, the main drivers of the present work are:

i.   to discuss the CFD analysis performed on the spinning foil;

ii.   to describe the force sensor sizing and manufacturing procedure;

iii.   to detail the mechatronic system designed to generate the fin motion

and to acquire the strain gauges signals;

iv.   to compare the measurements with the CFD results in order to validate

the numerical predictions.

After a description of the available water flume, Section 2 is dedicated to the

CFD analysis performed on the oscillating foil while Section 3 shows how the numerical

predictions guided the sizing of the force sensor. Section 4 details the transmission

system designed to generate the foil motion and shows the control and acquisition

platform of the experimental setup. Lastly, in Section 5, the measurements are

compared to the numerical predictions. Conclusions and future works are also discussed

in a further Section.

2. COMPUTATIONAL FLUID DYNAMICS ANALYSIS

Computational fluid dynamics represents an invaluable tool to assess the

propulsive performances of biomimetic thrusters. In this work, the numerical

simulations have been performed using an in-house developed research code named

MIGALE, based on the Discontinuous Galerkin (DG) space discretization [23,24]. DG

methods are variational methods, which combine features of the finite elements, such

as the elementwise polynomial representation of the solution, and of the finite volumes

as well, like the computation of the numerical fluxes at the mesh element interfaces.

Therefore, DG methods can provide very accurate solutions on curved and possibly

hybrid computational grids.

Here, the authors have employed the two-dimensional and incompressible version of the DG code, suitably extended to deal with a moving reference frame [25] to account for the fin oscillation: in this way, the computational complexity of the solving algorithm is reduced when compared to the dynamic mesh boundary condition commonly used in commercial CFD codes. The two-dimensional mesh has been created using about 4670 elements, suitably curved to represent the foil leading edge: figure 2 shows that the mesh is finer near the foil surface as well as along its wake. Fifth-order polynomials have been used to represent the solution within each element, resulting in a sixth-order space discretization while the time step size has been set equal to one thousandth of the foil oscillation period to ensure the results to be independent of the time discretization. Finally, a multi-core (32 processors) parallel computer system has been used to compute the numerical solution, taking about 32-48 hours to complete each simulation.

The numerical analysis has been performed on a NACA 0015 foil. The boundary conditions have been set in order to match those of the experimental tests: particularly, the freestream velocity equals that of the water flume, as well as the fluid density and viscosity. As stated before, two-dimensional flow has been computed, so the numerical analysis did not take into account the presence of the channel bottom wall and the water free surface. The same considerations stand for the flume lateral walls, meaning that an unbounded flow has been simulated. This choice will affect the sizing of the foil chord, thickness and span, as it will be showed in Section 3. In other words, the foil

should be sufficiently small in order to be unaffected by the presence of the flume walls and the water free surface.

Figure 3 shows the propulsive efficiency η and the average thrust coefficient, both predicted by the CFD analysis and displayed as a function of the Strouhal number St, a fluid dynamics parameter used to characterize oscillating flow phenomena; for an ostraciiform swimmer, St is defined as:

$$St = f\frac{A}{U} = f\frac{2c\sin\theta_0}{U} \tag{1}$$

where U is the incoming flow velocity, f is the foil oscillation frequency and A is the width of its wake, usually expressed in terms of foil chord c and oscillation amplitude θ_0 as done in (1). Here, θ_0 has been fixed to 15°, which corresponds to the optimal behaviour of the thruster, as demonstrated in [10]. The thrust coefficient, as commonly done in fluid mechanics to calculate the dimensionless force and torque values, has been computed by dividing the predicted thrust by the flow dynamic pressure and by the foil chord and span. The propulsive efficiency showed in figure 2 is known as Froude efficiency and it is defined as:

$$\eta = \frac{\langle T \rangle}{\langle P \rangle} U \tag{2}$$

where the numerator is the average thrust in an oscillation period, multiplied by the flow speed U, while the denominator is the averaged power required to spin the foil. The analysis have been focused in the $0.2 - 0.9$ range for St, where the efficiency peak is expected [26]. As shown in figure 3, two different conditions have been simulated: in the former, the rotation axis passes through the foil at 5% of its chord, while in the

latter, it passes at 25%. Figure 2 shows that the average thrust coefficient is higher when the rotation axis is closer to the foil leading edge.

3. FORCE SENSOR DESIGN

As stated in Section 1, the experimental setup proposed in this paper consists of an oscillating NACA foil suspended in a constant velocity freestream in a water flume. The foil shaft is connected to the transmission mechanism, which is placed above the water level, in a cantilever beam configuration, as shown in figure 1. The water flume is a 10 meters long straight channel with a rectangular section measuring 330 mm wide x 300 mm deep and provided with a recirculating pump. The flow velocity can be set between 120 mm/s and 150 mm/s by varying the inclination of the channel. However, since the water flow rate must remain constant due to the principle of mass conservation, its hydraulic head subsequently varies: 220 mm at 120 mm/s and 180 mm at 150 mm/s.

Dimensionless force C_F and torque C_M for a rectangular planform are typically expressed as:

$$C_F = \frac{2F}{\rho U^2 cb} \qquad C_M = \frac{2M}{\rho U^2 c^2 b} \tag{3}$$

where F and M are the measured forces and torque, ρ is the water density and b is the foil span; chord c and flow velocity U have already been defined in (1). The values of C_F and C_M obtained from the experiments can be compared with the force and torque coefficients computed by CFD in order to validate the simulations. On the other hand, (3) can be inverted to estimate the expected values of F and M using the coefficients C_F

and C_M predicted from CFD, as explained in Section 2. Regarding the values of U, c and b, the following considerations can be stated:

  i.   one span b must be left between the foil upper surface and the water free surface as well as between the foil lower surface and the tunnel bottom wall, in order to minimize the flow disturbances as stated in Section 2 - thus, the foil span b has been chosen equal to one-third of the hydraulic head as in figure 1;

  ii.   the foil aspect ratio which, for a rectangular planform, is equal to the ratio of span b to chord length c, must be greater than 3 in order to match the two-dimensional flow condition adopted in the numerical simulations, as stated in Section 2;

  iii.   freestream velocity U and hydraulic head are related by the principle of mass conservation.

$$b = \frac{H}{3} \qquad \frac{b}{c} \geq 3 \qquad Uh \approx cost$$

$$F = \frac{1}{2}\rho U^2 C_F cb \qquad M = \frac{1}{2}\rho U^2 C_M c^2 b$$

(4)

where H is the water flume hydraulic head. Thus, the optimal values of U, c and b can be computed by maximizing the forces and torques expressed in (4) by inverting (3). Indeed, under the same force and torque coefficients, the higher the propulsive loads, the easier the measurement of the aforementioned quantities. As expected, since the dynamic pressure depends from the square of the freestream velocity, the optimal value of U is equal to the maximum available, while the other parameters can be

calculated using the expressions in (4). Table I reports their final values. Given the value

of the foil chord, the width of the wake A, already defined in (1), is equal to 10 mm,

which is between one and two orders of magnitude smaller than the water flume width.

Thus, the unbounded flow condition, simulated in the CFD analysis, has been obtained

also in the experimental setup.

As previously stated, the experimental setup proposed in this paper exploits the

deflection and twisting of the foil shaft to measure the propulsive loads applied to the

foil itself. Thus, in order to achieve this result, a compliant element – namely, the force

and torque sensor – must be inserted along the rigid shaft, as shown in figure 1. The

ideal position for this element is right below the transmission system in order to

maximize the moment arm and thus amplify the effect of the applied loads. Since the

foil is attached to the transmission mechanism in a cantilever configuration, it is

immediate to solve the statically determined problems of bending and twisting as a

function of the expected loads F, M and then size the force sensor. Indeed, once the

loads along the shaft are known, the following step is the sizing of the compliant

element and the choice of its material: in this work, the tubular, thin-walled shape has

been chosen because it represents the best solution in terms of stress solving, symmetry

and manufacturing. Therefore, the maximal normal and shear strains due to bending

and twisting, namely ε_{max} and γ_{max}, on the measurement section can be computed as:

$$\varepsilon_{max} = \frac{FL}{EI}R \qquad \gamma_{max} = \frac{M}{GJ}R \tag{5}$$

where R is the cross-section outer radius, I and J are the area and polar moment of

inertia, E and G are Young's and shear modulus of the sensor material, while L is the

distance from the application point of the propulsive force F, which has been applied to

the trace of the rotation axis on the foil mid-section. Regarding the material choice,

since the order of magnitude of the expected loads varies between 10^{-2} and 1 N as a

function of the oscillation frequency, a sufficiently compliant material, such as plastics,

must be selected. Both Nylon and PVC are valid candidates due to their low elasticity

modulus: however, since PVC is more fragile than Nylon, the latter has been chosen to

manufacture the force sensor.

In order to size the sensor cross-section, namely its inner and outer radius r and

R, together with the distance L between the measurement section and the propulsive

forces application point, the following constraints need to be applied: first, the

deflection and twisting of the force sensor due to the applied loads F and M must be

small enough so that the foil resulting motion reasonably approximates a pure

oscillation. For a cantilever beam, the deflection δ due to the propulsive forces F and the

angle of twist ψ due to the applied torque M, both computed in the foil mid-section, can

be expressed as:

$$\delta = \frac{FL_S^3}{3EI} + \alpha_S\left(L_R + \frac{b}{2}\right) \ll A = 2c\sin\theta_0 \qquad \psi = \frac{M}{GJ}L_S \ll \theta_0 \tag{6}$$

where L_S and L_R are respectively the lengths of the force sensor and of the foil rigid

shaft, while α_S is the rotation of the clamping section, i.e. where the sensor is attached

to the rigid shaft. Equation (6) states that the maximum deflection δ must be

significantly smaller than the width of the foil wake A. Similarly, the second row of (6)

states that the maximum angle of twist ψ must be smaller than the oscillation amplitude

θ_0.

According to swim mechanics, the propulsive force is normally decomposed in its thrust and sway components, where the former is aligned to the freestream velocity vector, while the latter is normal. These directions identify the x and y axes of the ground frame showed in figure 4a. The force coefficients predicted by CFD analysis are already expressed according to the thrust-sway convention.

Figure 4b shows a possible arrangement of the strain gauges in a bending beam [27]; indeed, bending produces positive strain on a side of the beam and a negative strain on the opposite. With mirror-imaged or circular cross-sections, such as those of the force sensor proposed by the authors, the positive and negative strains have the same magnitude: it is then possible to exploit the features of the Wheatstone bridge for the addition of the strain signals. Namely, when a full bridge configuration is used, the thermal and pure tensile strains are compensated, while the indicated strain due to bending is amplified four times. Here however, the strain gauges are attached to sensor outer surface as shown in figure 1, which is fixed to the spinning shaft. Thus, called n the axis normal to the sensored faces of figure 4b, the measured bending strains are due to the projection of the thrust and sway forces in the n-direction, as displayed in figure 4a. Therefore, in order to recompose the propulsive force components acting in the x-y directions of the ground frame, it is necessary to measure the bending strain in the perpendicular directions n and c of the sensor frame, as shown in figure 1 and figure 4b. Hence, eight strain gauges – four for each direction of the sensor frame – are necessary to solve the static problem of the loads applied to the foil, once its relative orientation θ

with respect to the freestream direction has been determined. That's the purpose of the camera sensor in figure 1, as it will be shown in Section 4.

Figure 5 shows two alternative layouts for the aforementioned strain gauges: the cylindrical surface of the tubular sensor has been projected on a plane, while the vertical lines are spaced by a 90 degrees rotation, thus identifying the four sides of the beam in figure 4b. Therefore, two strain gauges must be attached close to a line, representing the couple SG1-SG3 of figure 4b, while the remaining SG2-SG4, necessary to complete the full bridge, are fixed to the line spaced by a 180 degrees rotation from the former. By adopting the parallel arrangement on the left, the strain gauges of each bridge measure the deformation in the same cross-section; on the contrary, the aligned layout on the right is more compact. Thus, the latter has been chosen as the strain gauges arrangement to minimize the cross-section diameter and suit the sensor compliancy to the expected loads.

The strain gauges in figure 5 are of the uniaxial type, meaning that they measure the deformation only in the direction of their grid. Although more complex types actually exist, the uniaxial ones are the most compact and narrow, thus perfectly suited to the present application. Particularly, the KFG 120 by Kyowa (GF 2.1) have been selected for the bending strains: their grid is just 1.4 mm wide, 2.8 considering their bonding base. Therefore, the encumbrance of four strain gauges of the selected type, placed in the aligned arrangement of Figure 4, is 11.2 mm. Since manufacturing issues about the bonding phase advice against reducing the section outer diameter below 10 mm, this value has been selected for the force sensor proposed in this work.

Consequently, the associated circle measures 31.4 mm, more than enough to house four strain gauges of the selected type. Besides, the length of the sensor L_S can be estimated according to the Saint-Venant Principle and from the specifications on bending strain gauges installation: indeed, in order to avoid that stress concentrations due to the clamping forces applied to the constrained sections – where the sensor is connected to the transmission mechanism and to the rigid shaft – affect the measurement, a distance equal to three times the sensor outer diameter must be left from both sides of the measurement area. Then the force sensor length is equal to 70 mm: 10 mm for the couple of aligned strain gauges of figure 5 and 30 mm over and below the measurement area.

The last step of the sizing procedure is the selection of the sensor inner diameter: a first guess is 9 mm, which is simple to achieve by means of a lathe machining. Once its material and geometry have been chosen, distances L and length L_R can be calculated by means of (5) and (6) as a function of the loads F and M: particularly, since the propulsive forces depend from the oscillation frequency f as shown by figure 3, it is opportune to vary length L_R according to the spinning speed. In this way, the bending strains are higher than the lower bound of deformations for the selected strain gauges, which is equal to 10 microstrains, while the deflections of the sensor δ are lower than the acceptable values stated by (6). For example, L_R is equal to 300 mm at 2 Hz and 210 mm at 3 Hz.

Regarding the twisting torque M, the possibility to measure the applied torque does not depend from any length. Then, it is sufficient to verify that the shear strains

due to M are greater than 10^{-5} for the guessed thickness, while the twisting angles ψ

remains lower than the value stated by (6), which results true when f belongs to the

range 2–4 Hz. The strain gauges adopted to measure M are two torque rosette, series

062uv, by Vishay (GF 2.09).

4. MECHATRONIC SYSTEM DESIGN AND MANUFACTURING

The required fin motion law in ostraciiform locomotion is of the type:

$$\theta = \theta_0 \cos(2\pi f t) \tag{7}$$

In [1], the authors have designed a transmission mechanism based on a spatial-

cam kinematic joint, which converts the continuous rotation of its drive in the harmonic

oscillation of the output member. The mechanism is displayed in figure 6: the output

angle θ and the drive rotation φ are then related by the expression:

$$\tan \theta = \frac{h}{l} \cos \varphi \qquad \varphi = 2\pi f t \qquad \frac{h}{l} = \tan \theta_0 \tag{8}$$

where h and l are the geometric parameters outlined in figure 6. Equation (8) slightly

differs from the law of motion (7); still, it results easy to show that (8) approximates a

pure sinusoidal function if $h/l <\!\!<1$, which is true for θ_0 equal to 15 degrees, as in the

experimental setup proposed in this work.

In addition to the transmission mechanism, the mechatronic system is composed

by a brushed DC motor with its driver and a National Instruments MyRIO board,

featuring a Linux real-time System on Module (SOM) with an embedded dual core ARM

Cortex-A9 processor and Xilinx Z-7010 FPGA Module. The MyRIO SOM is employed both

as the system controller and as its acquisition device: namely, it allows to synchronize

the video recording device displayed in figure 1, which consists of a GoPro Hero 5 camera, with the rest of the system. At the same time, the MyRIO-1900 Expansion Port MPX connectors allows the board to acquire both the feedback signals from the motor encoder and the measurement signals from the strain gauges. The whole software has been developed in NI LabVIEW. Particularly, it is composed by two real-time loops running in parallel and dedicated to two different purposes: the control loop and the acquisition loop. The control loop has a classical state-machine architecture; its main function is to control the motor in order to adjust its frequency to the value set from the user, by means of a PI controller. On the other hand, the acquisition loop has a producer and consumer architecture: data gathered through the analogue input channels at high speed are stored in a queue from the producer loop and then are passed to the slower consumer loop in order to be processes and saved in an external memory storage unit. The acquisition loop starts when a trigger button is pushed by the user: this very action simultaneously activates a dedicated SubVI through which the record start command is sent, through the Wi-Fi connection, to the GoPro camera.

As stated in Section 3, the synchronization between the recording device and the measurement signals is due to the necessity to project the loads measured along the axes of the sensor frame, in those of the ground frame, i.e. in the thrust-sway directions. The recorded video is then processed by a dedicated software called Kinovea, which automatically extracts the foil angular position from the images; the obtained values are then associated to the corresponding force and torque measurement by the control software running on the MyRIO board.

Regarding the manufacturing and assembly processes, both the foils and many other components of the transmission system described in this Section have been printed by high-resolution stereolithography (SLA). Particularly, the adopted 3-D printing technique allows the fabrication of closed and hollow parts: this option has been exploited both to minimize the magnitude of the inertia forces with respect to the applied propulsive loads as well as to manufacture statically balanced foils by removing the material behind the rotation axis, where the majority of its mass is distributed.

The force sensor sized in Section 3 has been manufactured from a Nylon rod by lathe. Particularly, the clamping sections have twice the diameter of the sensor in the measurement area, with chamfered edges where the wider section joins the narrower in order to avoid stress concentrations. Once the flexible shell has been produced, the strain gauges have been positioned on the sensor outer surface using an alignment grid and then bonded in their own slot by means of a cyanoacrylate adhesive. The final assembly of the force sensor adopted in this work is displayed in figure 7: here, the cyan, red, white and black wires identify the four legs of the Wheatstone bridge circuits realized for the bending strain gauges and for the torque rosette as well. Three groups of bondable, printed-circuit terminal pads (BTPs) have been employed to connect the primary leadwire of the bridge circuits to the delicate jumpers of the strain gauges. Figure 8 shows the final assembly of the proposed experimental setup.

Before starting the tests, the force sensor has been properly calibrated for pure bending and twisting using known weights: a steel support has been thus attached to a clamping section in order to position the weights at a known distance from the

measurement section. The same procedure has been followed to calibrate the torque

rosettes. Figure 9 shows the trends of the calibration curves. Cross-talk between the

individual groups of strain gauges has been also measured in this phase and then

mathematically compensated by the inverse-matrix method [27]: the force sensor has

been thus connected to three oscilloscopes while pure bending and torque loads have

been applied, measuring a cross-talk output between 1 and 5%. Once the linear problem

of cross-talk has been properly formulated, its matrix has been inverted in order to

obtain the cross coupling coefficients and thus remove the undesired output. This

procedure has also allowed to set the amplification factor of the employed amplifier in

order to obtain a measurement signals suited to the ± 10 V differential analog input

channels of the acquisition platform.

5. EXPERIMENTAL RESULTS

The tests have been conducted at three different oscillation frequencies inside to

the 2-4 Hz range, as shown in Table II together with the corresponding Strouhal values,

computed when the foil rotation axis intersects its midsection at 5% of its chord and at

25%. As stated in Section 3, when the frequency is minor than the lower bound, the

strain gauges are affected by noise disturbances; on the other hand, when the

frequency is higher than the upper bound, the twisting angle due to the propulsive

torque M is no longer negligible with respect to the oscillation amplitude θ_0. Given the

highest frequency value in Table II, the real-time control, synchronization and

acquisition loops are executed every 10 ms by the MyRIO board, twenty-five times

faster than the upper bound of the prescribed range.

Functional tests have been performed on the components of the experimental

setup. First, the performances of the GoPro Hero 5 camera have been properly

investigated: several videos have been thus recorded to test the possibility to produce

clear images even at the highest oscillation frequency. By setting the camera at 240

frames per second, the authors have been able to reconstruct the foil angular position

by tracing the trajectory of a couple of white spots drawn on the fin upper surface, as

shown in figure 10. As stated before, the videos have been processed using an open

source software named Kinovea. The fin angular position measured at five different

frequencies has been compared with the pure sinusoidal functions of time in (7) and the

highest deviation between the desired and the actual trend has resulted equal to 12% at

the highest oscillation frequencies [28].

Figure 11 and Table III show the Normalized Error *NE* between the force and

torque coefficients computed by CFD and those obtained from the experiments,

displayed as a function of the Strouhal numbers of Table II. The aforementioned

quantities have been calculated as:

$$NE = \frac{\sqrt{\sum (s_i - e_i)^2}}{\sqrt[4]{\sum (s_i)^2 \ \sum (e_i)^2}} \tag{9}$$

where s_i and e_i are respectively the simulated and experimental coefficients at the same

instant of time. Their trends are also displayed in Figure 12 (a)-(t). The experimental

curves are always lower than their simulated counterparts, an expected feature of the

finite volumes method. The known contribution of the inertia forces and torque has

been subtracted from the measurements before the projection of the propulsive loads

in the thrust-sway directions. The three curves of figure 11 show a decreasing-increasing

behavior and the normalized error NE between the CFD and experimental coefficients is

minimal when the Strohual number is 0.54, which corresponds to a 3.5 Hz oscillation

frequency when the rotation axis crosses the foil midsection at 25% of its chord. As

stated in [20], the propulsive loads grow with the square of St, as also shown in figure 3.

This evidence suggests a possible interpretation of the trends in figure 11: when St is

lower than the aforesaid value, the propulsive loads, particularly the thrust force and

the torque, are small enough to generate deformations in a range where the strain

gauges are slightly affected by noise disturbances. Indeed, despite the efforts made to

manufacture a force sensor complying with the specifications stated in the design

phase, the presence of the BTPs, of the adhesive remains and of the circuits wires could

have slightly affected the sensor stiffness, resulting in a higher value which, in turn,

corresponds to lower strains. As St grows past 0.6, the rising loads applied to the foil

generate deflections and twists large enough that its resulting motion deviates from a

pure rotation, resulting in a distorted velocity field and thus different loads.

Furthermore, the following considerations about the CFD analysis need to be stated:

even if the velocity field predicted from the numerical method is most accurate, the

resulting stress field is always affected by a higher error due to the finite difference

approximation of the velocity spatial derivatives that the viscous stresses depend from.

Therefore, a modelling error of the order of 10% is expected in the computation of the

propulsive forces and torque acting on the fin [23]-[25].

Nevertheless, on the basis of the aforementioned considerations and considering the deviation in the foil angular position due to the image processing algorithm as well as the three-dimensional flow effects neglected in the numerical simulations, the normalized errors between the coefficients predicted by the CFD analysis and the non-dimensional forces and torque measured with the proposed experimental setup are reasonably acceptable inside the range of frequencies adopted in the tests. Indeed, the aim of the authors is to validate the numerical predictions not to simulate the complex, three-dimensional fluid-structure interactions of real fish swimming, which would require more powerful tools and longer computational time, but to investigate the reliability of fast method in order to run a comparative analysis of the propulsive performances of a moving foil in different kinematic conditions – which would be much more difficult with an experimental campaign - such as the type of motion and so on.

Once the numerical predictions have been validated, the last test conducted by the authors of this paper regarded the investigation of the propulsive benefits offered by a rigid and slender fish-like body fixed before of the oscillating foil, as shown in figure 13. Here, the mid-plane section of the body has been obtained from a NACA0015 foil; however, its aft part has been tapered in order to resemble the narrow peduncle of ostraciiform swimmers. The whole structure has then been manufactured by high-resolution stereolithography. Table IV shows a comparison between the propulsive performances of the spinning foil isolated in the freestream and the fish-like assembly: the experiments have demonstrated that the average thrust coefficient in an oscillating

period and the propulsive efficiency are respectively 2.6% - 9.8% and 0.6% - 2.7% higher

when a slender body is placed before the fin and its effect is more relevant as the

frequency rises. A possible explanation for this result is the following: as the Strouhal

number rises above the maximum efficiency peak, oscillating foils experience an

increase of the separate flow region occurring at their leading edges as shown in figure

14, which causes an efficiency drop due to the fact that the propulsive thrust grows

slower than the sway force component [29]. On the contrary, the presence of the

slender body before the stagnation point could actually reduce flow separation

phenomena in a way similar to the "undulating pump" mechanism described by Müller

et al [20]. This hypothesis will be further investigated as future work, by means of more

powerful computational fluid dynamics techniques.

6. CONCLUSIONS AND FUTURE WORKS

Bio-inspired solutions are currently investigated as a source of improvement for

autonomous underwater robots. CFD and measurement techniques have improved the

understanding of the complex fluid-structure interaction underlying biological

locomotion. Still, the predicted results must be validated.

This paper presents the experimental validation of the CFD analysis performed

on an oscillating foil. The core of the system is a cantilever beam, strain gauges-based

force sensor, designed according to the simulations that the authors aimed to validate.

The adopted solution allowed the measurement of the bending and twisting moments

acting on the spinning shaft and thus to obtain the resulting forces and torque due to

the side pressure distribution. Once the mechatronic system has been correctly

assembled and preliminarily tested, propulsive loads measurements have been performed at three oscillation frequencies, both for an isolated spinning foil and in a fish-like assembly.

In the first case, as the oscillation frequency rises from 2 Hz to 3.5 Hz, the trends of the numerical curves becomes non-symmetrical due to the increasing effect of the initial conditions: indeed, since the flow regime is laminar, the wake behind the foil is twisted in the direction of the foil angular velocity at time equal to zero. Therefore, since the fluid dynamics forces and torque strongly depends from the vorticity field due to the array of vortices staggering in the wake [20], its asymmetric behavior affects the trends of the forces and torque within an oscillation cycle. Figure 12 shows that the curves representing the non-dimensional force and torque measured in the experiments, partially fail to follow the aforementioned asymmetric trends of the numerical ones: this is due to the mixing effect of the slightly turbulent flow in the water flume. Turbulence, as it is known, increases diffusivity and thus tends to homogenize fluid mixtures and currents, canceling the effects of the initial conditions. In the proposed experimental setup, turbulent flow is primarily due to the presence of the recirculating pump, the water free surface, the tunnel bottom wall and the recording device. However, despite the presence of such disturbances, the comparison between the numerical and the experimental curves as well as the calculation of the corresponding error show a good agreement between the simulated and measured loads.

The next steps of the project focus on the measurement of the propulsive loads generated by the flapping foils of the more efficient thunniform swimmers. Indeed, the aim of the authors is to pursue the highest possible propulsive efficiency for underwater locomotion by adopting bio-inspired solutions.

REFERENCES

[1] D. Scaradozzi, G. Palmieri, D. Costa, and A. Pinelli, "BCF swimming locomotion for autonomous underwater robots: a review and a novel solution to improve control and efficiency". Ocean Engineering, vol. 130, pp. 437-453, 2017.

[2] P. A. Zapata-Ramírez, D. Scaradozzi, L. Sorbi, M. Palma, U. Pantaleo, M. Ponti, and C. Cerrano, "Innovative study methods for the Mediterranean coralligenous habitats". Advances in Oceanography and Limnology, Vol. 4, no. 2, pp. 102-119, 2013.

[3] L. Sorbi, D. Scaradozzi, F. Zoppini, S. Zingaretti, and P. Gambogi, "Robotic tools and techniques for improving research in an underwater delicate environment". Marine Technology Society Journal, Vol. 49, no. 5, pp. 6-17, 2015.

[4] B. Allotta, et al, "The ARROWS Project: robotic technologies for underwater archaeology". In IOP Conference Series: Materials Science and Engineering, Vol. 364, no. 1, p. 012088. IOP Publishing, 2018.

[5] J. Wang, Y. Fei, and Z. Liu, "Locomotion modeling of a triangular closed-chain soft rolling robot". Mechatronics, Vol. 57, pp. 150-163, 2019.

[6] B. Liu, Y. Yang, F. Qin, and S. Zhang, "Performance study on a novel variable area robotic fin". Mechatronics, Vol. 32, pp. 59-66, 2015.

[7] J. Wang, and X. Tan, "A dynamic model for tail-actuated robotic fish with drag coefficient adaptation". Mechatronics, Vol. 23, No. 6, pp. 659-668, 2013.

[8] M. Holt, A. K. MacPherson, "Numerical Methods in Fluid Dynamics". ASME Journal of Dynamic Systems, Measurements and Control, Vol 100, No. 2, 161–162, 1978.

[9] I. Hbiri, H. Karkri, F. Ghorbel, and S. Choura, "Modeling and Parameter Identification of an In-Tank Swimming Robot Performing Floor Inspection". ASME Journal of Dynamic Systems, Measurements and Control, Vol 141, No. 3, 2018.

[10] D. Costa, G. Palmieri, D. Scaradozzi, and M. Callegari, "Multi-body Analysis of a Bio-Inspired Underwater Robot". In The International Conference of IFToMM ITALY, Springer, Cham, pp. 240-248. 2018.

[11] J. M. Anderson, K. Streitlien, D. S. Barrett and M. S. Triantafyllou, "Oscillating foils of high propulsive efficiency". Journal of Fluid Mechanics, vol. 360, pp 41-72, 1998.

[12] L. Schouveiler, F.S. Hover, and M. S. Triantafyllou, "Performance of flapping foil propulsion". Journal of Fluids and Structures, vol 20, no. 7, pp. 949-959, 2005.

[13] Y. J. Park, U. Jeong, J. Lee, S. R. Kwon, H. Y. Kim, and K. J. Cho, "Kinematic condition for maximizing the thrust of a robotic fish using a compliant caudal fin". IEEE Transaction of Robotics, vol. 28, no. 6, pp. 1216-1227, 2012.

[14] D. S. Barrett, M. S. Triantafyllou, D. K. P. Yue, M. A. Grosenbaugh, and M. J. Wolfgang, "Drag reduction in fish-like locomotion". Journal of Fluid Mechanics, vol. 392, pp. 183-212, 1999.

[15] P. Prempraneerach, F. S. Hover, and M. S. Triantafyllou, "The effect of chordwise flexibility on the thrust and efficiency of a flapping foil." 13th International Symposium on Unmanned Untethered Submersible Technology (UUST), New Hampshire, vol. 152, pp. 150-170, 2003.

[16] K. H. Low, C. W. Chong, and C. Zhou, "Performance study of a fish robot propelled by a flexible caudal fin". Robotics and Automation (ICRA), IEEE International Conference on, Anchorage, pp. 90-95, 2010.

[17] G. V. Lauder, E. J. Anderson, J. Tangorra, and P. A. Madden, "Fish biorobotics: kinematics and hydrodynamics of self-propulsion": The Journal of Experimental Biology, vol. 210, pp. 2767-2780, 2007.

[18] L. Wen, G. Wu, J. Liang, and J. Li, "Hydrodynamic experimental investigation on efficient swimming of robotic fish using self-propelled method". International Journal of Offshore and Polar Engineering, vol. 20, no. 3, 2010.

[19] S. Wang, G. He, X. Zhang, "Self-propulsion of flapping bodies in viscous fluids: recent advances and perspectives". Acta Mechanica Sinica, vol. 32, no. 6, pp. 980-990, 2016.

[20] M. Sfakiotakis, D. M. Lane, J. B. C. Davies, "Review of fish swimming modes for aquatic locomotion," IEEE Journal of Oceanic Engineering, vol. 24, no 2, pp. 237-252, 1999.

[21] W. L. Chan, T. Kang, and Y. J. Lee, "Experiments and identification of an ostraciiform fish robot". Robotics and Biomimetics (ROBIO), IEEE International Conference on, pp. 530-534, Sanya, 2007.

[22] P. Kodati, J. Hinkle, A. Winn, and X. Deng, "Microautonomous robotic ostraciiform (MARCO): hydrodynamics, design and fabrication". IEEE Transaction on Robotics, vol. 24, no. 1, pp. 105-117, 2008.

[23] F. Bassi, S. Rebay, "Numerical evaluation of two discontinuous Galerkin methods for the compressible Navier–Stokes equations". International journal for numerical methods in fluids, Vol. 40 (1-2), pp. 197-207, 2002.

[24] F. Bassi, A. Crivellini, D. A. Di Pietro, S. Rebay, "An implicit high-order discontinuous Galerkin method for steady and unsteady incompressible flows". Computers & Fluids, Vol. 36(10), pp. 1529-1546, 2007.

[25]   F. Bassi, L. Botti, A. Colombo, A. Crivellini, N. Franchina, A. Ghidoni, "Assessment of a high-order accurate Discontinuous Galerkin method for turbomachinery flows". International Journal of Computational Fluid Dynamics, Vol. 30, no. 4, pp. 307-328, 2016.

[26] C. Eloy, "Optimal Strouhal number for swimming animals", Journal of Fluids and Structure, Vol. 30, pp. 205-208, 2012.

[27] K. Hoffmann, "An introduction to stress analysis and transducer design using strain gages". HBM, www.hbm.com, 2012.

[28] D. Costa, G. Palmieri, M. Callegari, D. Scaradozzi, G. Zitti, M. Brocchini, "Experimental Setup for the Validation of the Bio-Inspired Thruster of an Ostraciiform Swimming Robot". In 2018 14th IEEE/ASME International Conference on Mechatronic and Embedded Systems and Applications (MESA), (pp. 1-6). IEEE.

[29] D. Costa, M. Franciolini, G. Palmieri, A. Crivellini, D. Scaradozzi, "Computational Fluid Dynamics Analysis and Design of an Ostraciiform Underwater Robot". Proceedings of the 2017 IEEE International Conference on Robotics and Biomimetics, ROBIO, Macau, pp. 5-8, 2017.

Figure Captions List
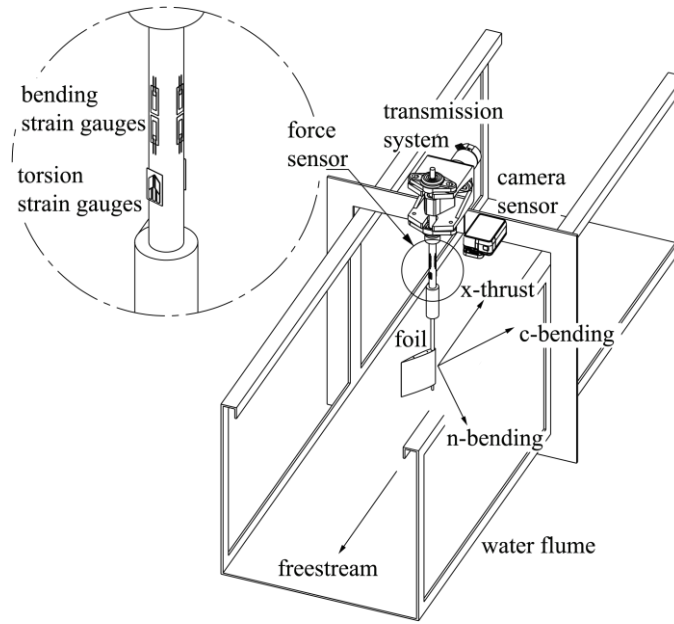
Fig. 1   Experimental setup and force decomposition

Fig. 2   Mesh used in the CFD analysis

Fig. 3   Predicted Thrust coefficient and Froude Efficiency [1] as a function of the
                Strouhal number with $\theta_0 = 15°$ and Reynolds equal to 3000

Fig. 4   Axes convention in swim mechanics. (a) Strain gauges arrangement in a
                bending beam [27]. (b)

Fig. 5   Alternative layouts for the bending strain gauges: parallel (left), aligned
                (right)

Fig. 6   Transmission mechanism based on a spatial-cam joint [1]

Fig. 7   Final assembly of the force sensor

Fig. 8   Final assembly of the experimental setup

Fig. 9   Calibration curves of the force sensor

Fig. 10   Foil picture acquired by GoPro camera processed by Kinovea

Fig. 11   Trends of the Normalized Error between the experimental and the
                simulated force and torque coefficients.

Fig. 12   Comparison between the coefficients computed by the CFD analysis and
                the non-dimensional forces and torque measured in the tests: (a), (b), (c)
                is 2 Hz at 5%; (d), (e), (f) is 2 Hz at 25%; (g), (h), (i) is 3 Hz at 5%; (l), (m),
                (n) is 3 Hz at 25%; (o), (p), (q) is 3.5 Hz at 25%; (r), (s), (t) is 3.5 Hz at 25%.

Fig. 13   Experimental setup in the fish-like assembly

Fig. 14   Flow visualization around an oscillating plate at St = 1.1 [28]

Table Caption List

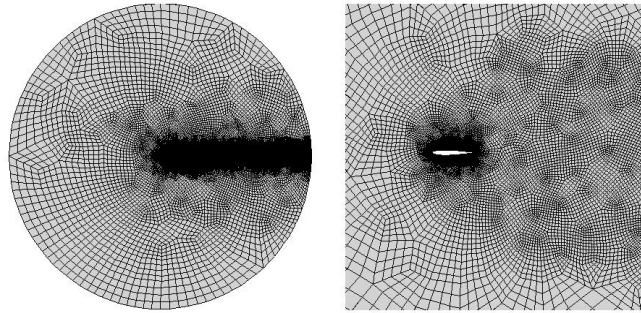Figure 1. Experimental setup and force decomposition.
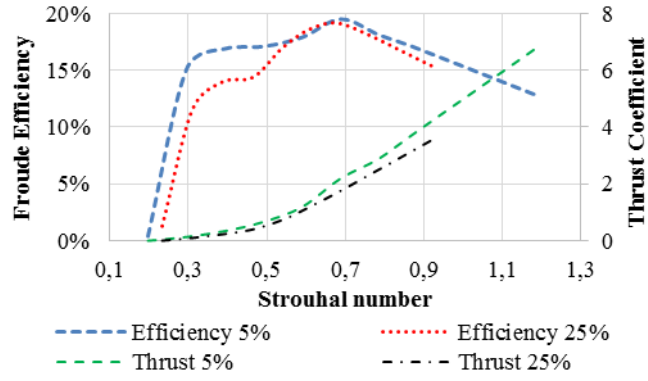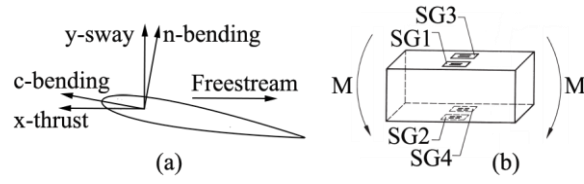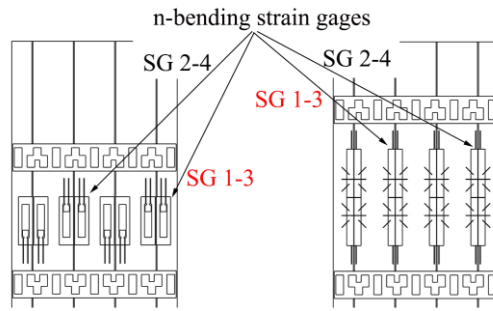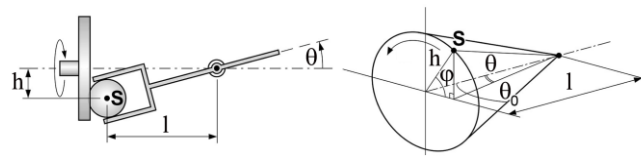
Figure 2. Mesh used in the CFD analysis.

Figure 3. Predicted Thrust coefficient and Froude Efficiency [1] as a function of the Strouhal number with $\theta_0 = 15°$ and

Figure 4. Axes convention in swim mechanics. (a) Strain gauges arrangement in a bending beam [27]. (b)

Figure 5. Alternative layouts for the bending strain gauges:
parallel (left), *aligned* (right)

Figure 6. Transmission mechanism based on a spatial-cam
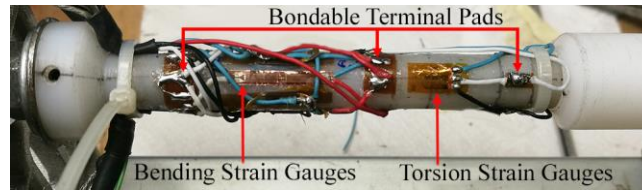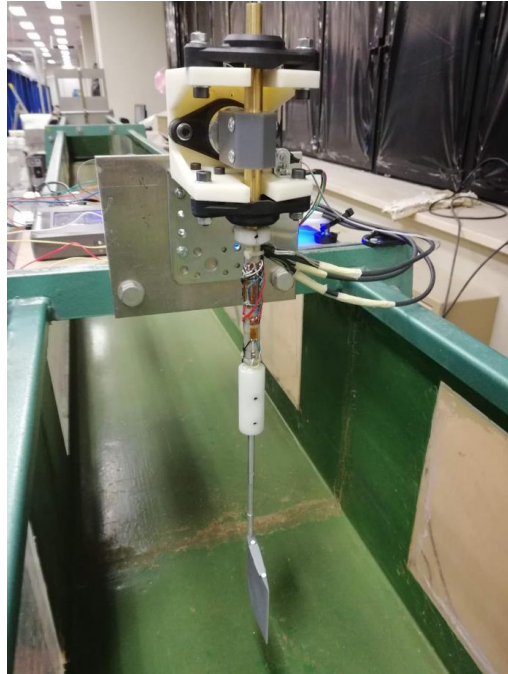
Figure 7. Final assembly of the force sensor.

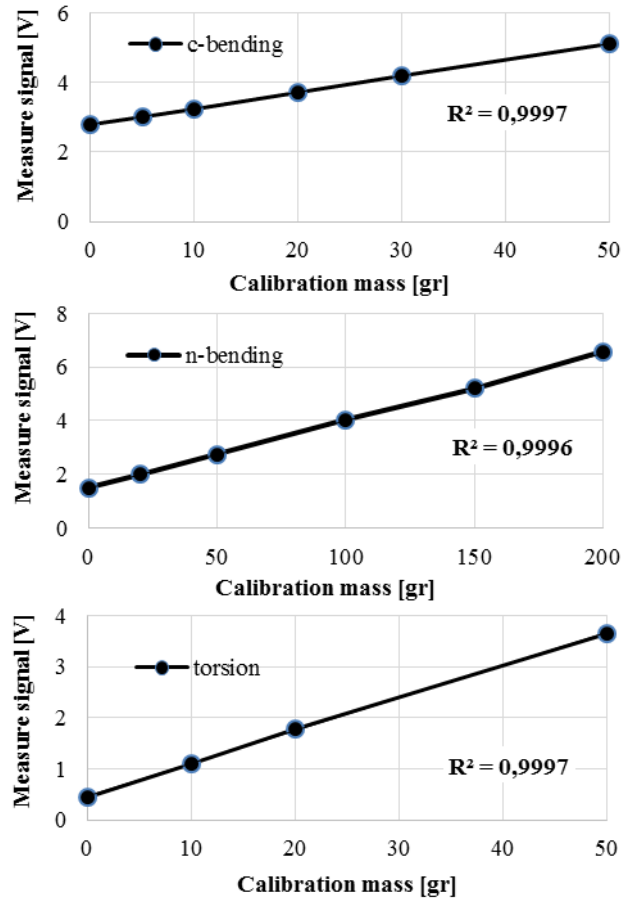Figure 8. Final assembly of the experimental setup.

Figure 9. Calibration curves of the force sensor.

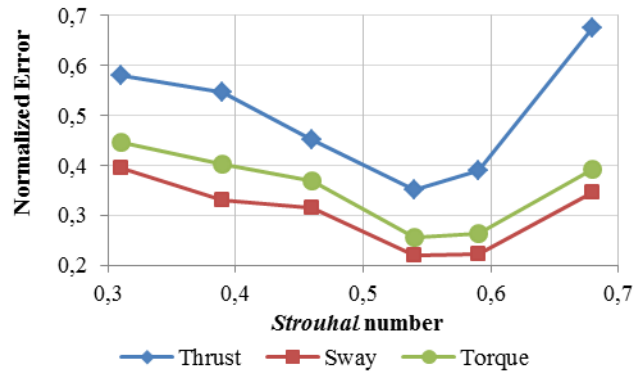Fig. 10. Foil picture acquired by GoPro camera processed by

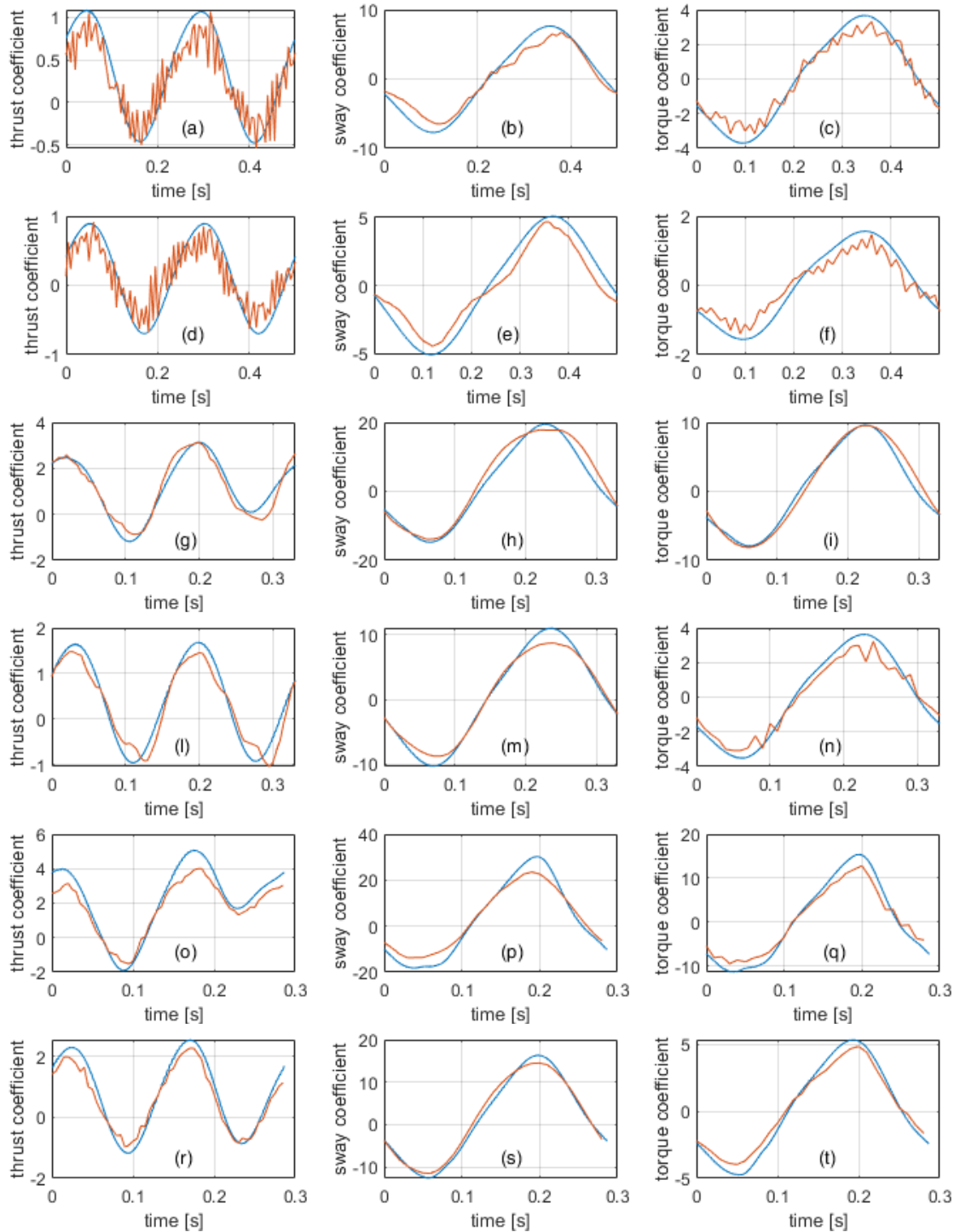Figure 11. Trends of the Normalized Error between the

Fig. 12. Comparison between the coefficients computed by the CFD analysis and the non-dimensional forces and torque measured in the tests: (a), (b), (c) is 2 Hz at 5%; (d), (e), (f) is 2 Hz at 25%; (g), (h), (i) is 3 Hz at 5%; (l), (m), (n) is 3 Hz at 25%; (o), (p), (q) is 3.5 Hz at 25%; (r), (s), (t) is 3.5 Hz at 25%.

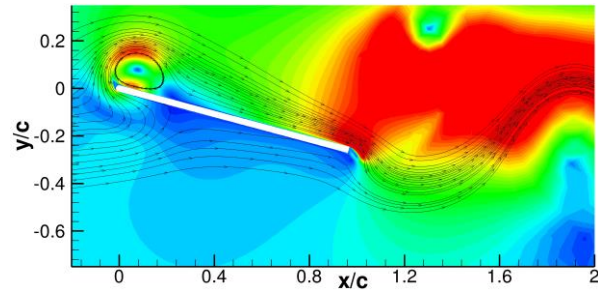Fig. 13. Experimental setup in the fish-like assembly.

Fig. 14. Flow visualization around an oscillating plate at St = 1.1 [28].

TABLE I
PARAMETERS OF THE EXPERIMENTAL SETUP

U [mm/s]	b [mm]	c [mm]	Reynolds
150	60	20	3000

TABLE II
FOIL OSCILLATION FREQUENCIES DURING THE TESTS

Frequency [Hz]	2	3	3.5
Strouhal (5%)	0.39	0.59	0.68
Strouhal (25%)	0.31	0.46	0.54

TABLE III
NORMALIZED ERROR (NE) BETWEEN THE EXPERIMENTAL
AND THE NUMERICAL CURVES

Strouhal number	0.31	0.39	0.46	0.54	0.59	0.68
Thrust force NE	0.580	0.546	0.452	0.352	0.388	0.675
Sway force NE	0.393	0.331	0.315	0.219	0.223	0.346
Torque NE	0.445	0.403	0.368	0.256	0.263	0.393

TABLE IV
PROPULSIVE PERFORMANCES IN THE ISOLATED AND FISH-LIKE CONDITIONS

Strouhal number	0.39		0.59		0.68	
Assembly	Isolated	Fish-like	Isolated	Fish-like	Isolated	Fish-like
Thrust coefficient	0.304	0.312	1.045	1.159	1.953	2.146
Propulsive efficiency	15.8%	15.9%	16.8%	17.1%	18.9%	19.4%